PCCP

ROYAL SOCIETY OF CHEMISTRY

PAPER

View Article Online
View Journal | View Issue

Cite this: *Phys. Chem. Chem. Phys.*, 2020, **22**, 26265

Ab initio metadynamics calculations of dimethylamine for probing pK_b variations in bulk *vs.* surface environments†

Sohag Biswas,[a] Hyuna Kwon,[a] Kelley C. Barsanti,[a] Nanna Myllys,[b] James N. Smith[b] and Bryan M. Wong *[ac]

Received 19th July 2020,
Accepted 3rd November 2020

DOI: 10.1039/d0cp03832f

rsc.li/pccp

The basicity constant, or pK_b, is an intrinsic physical property of bases that gives a measure of its proton affinity in macroscopic environments. While the pK_b is typically defined in reference to the bulk aqueous phase, several studies have suggested that this value can differ significantly at the air–water interface (which can have significant ramifications for particle surface chemistry and aerosol growth modeling). To provide mechanistic insight into surface proton affinity, we carried out *ab initio* metadynamics calculations to (1) explore the free-energy profile of dimethylamine and (2) provide reasonable estimates of the pK_b value in different solvent environments. We find that the free-energy profiles obtained with our metadynamics calculations show a dramatic variation, with interfacial aqueous dimethylamine pK_b values being significantly lower than in the bulk aqueous environment. Furthermore, our metadynamics calculations indicate that these variations are due to reduced hydrogen bonding at the air–water surface. Taken together, our quantum mechanical metadynamics calculations show that the reactivity of dimethylamine is surprisingly complex, leading to pK_b variations that critically depend on the different atomic interactions occurring at the microscopic molecular level.

1 Introduction

The formation and growth of atmospheric aerosol particles play an important role in global climate through the formation of clouds and scattering of solar radiation.[1–3] Under ambient conditions, sulfuric acid molecules accelerate new particle formation (NPF) in the atmosphere,[4–7] particularly when they collide with molecules having a high basicity in the lower atmosphere. At the atomistic level, theoretical models[8–11] and measurements[12–15] have shown that amines, such as dimethylamine, can form strong bonds with sulfuric acid and can be more effective at particle formation than ammonia due to their higher basicity.[16–18] In this respect, dimethylamine can behave as a ''superglue'' since interactions with sulfuric acid result in the formation of stable clusters that are more likely to grow than evaporate.

Although it has been demonstrated that the reaction of dimethylamine with sulfuric acid is important for NPF, there is both a theoretical and experimental ''blind spot'' in our understanding of the evolution nanoparticles formed from this system. In laboratory measurements performed at the CLOUD chamber at CERN, nucleated clusters appear to be composed of bisulfate (protonated dimethylamine-to-sulfate ratio of 1) that trends towards a fully neutralized salt (ratio of 2) with increasing cluster size.[19] In contrast, 10 nm diameter particles formed from these clusters during the same experiments were observed to have much lower concentrations of protonated dimethylamine relative to sulfate (ratio of 0.2), which trended towards a fully neutralized condition once particles grew to 20 nm in diameter.[20] It is not clear how the observed base-to-acid ratio in clusters connect to that observed in the smallest measured nanoparticles. To address this discrepancy, an in-depth understanding of the underlying proton-transfer mechanisms that are relevant to dimethylamine-mediated NPF at the atomistic scale is needed. Atomistic studies of dimethylamine would allow a better understanding and model representation of proton-transfer at the particle–surface and in the bulk phase, including surface effects or confined conditions. While compound physical–chemical properties are well understood under bulk conditions, such

[a] *Department of Chemical & Environmental Engineering, University of California-Riverside, Riverside, California 92521, USA. E-mail: bryan.wong@ucr.edu; Web: http://www.bmwong-group.com*
[b] *Department of Chemistry, University of California-Irvine, Irvine, California 92697, USA*
[c] *Materials Science & Engineering Program, Department of Chemistry, and Department of Physics & Astronomy, University of California-Riverside, Riverside, California 92521, USA*

† Electronic supplementary information (ESI) available: Additional computational details on metadynamics calculations and convergence tests. See DOI: 10.1039/d0cp03832f

properties are not well characterized under confined conditions (such as in a cluster or on a surface). Specifically relevant for this work, while the conventional definition of the basicity constant, pK_b, is defined in reference to the bulk aqueous phase, several studies have suggested that this value can differ significantly at the air–water interface.[21–24]

To accurately probe these confinement effects, the use of *ab initio* molecular dynamics (AIMD) simulations is required since both the solute and solvent molecules are treated at a quantum mechanical level of detail.[25] However, the use of AIMD calculations for weak bases in aqueous environments is not routine since the protonation of these molecules is a rare event that requires exceptionally long simulation times (which further adds to the already immense computational cost of quantum mechanical calculations). To address this issue, the metadynamics formalism used in this work provides an efficient approach for investigating these rare events by preventing the system from revisiting regions of configuration space that have already been previously explored.[26] Using these metadynamics calculations, we explore the free-energy profile of dimethylamine protonation to provide trends in the computed pK_b in various solvent environments. As such, this work provides detailed mechanistic insight and presents the first quantum-based metadynamics simulation of dimethylamine in confined aqueous environments for understanding these intricate dynamical effects.

2 Computational details

2.1 AIMD simulations

The QUICKSTEP[27–29] module in the CP2K program[30,31] was used to perform all of the *ab initio* molecular dynamics simulations in this study. The QUICKSTEP method in CP2K employs hybrid Gaussian and plane-wave (GPW)[32] schemes for the efficient calculation of forces and energies. GTH pseudopotentials[33,34] were used to describe the atomic core electrons, and the Kohn–Sham orbitals for the valence electrons utilized the TZV2P[35] basis set. Our simulations utilized the BLYP[36–38] functional in combination with D3 dispersion corrections,[39] and a 6 Å cut-off radius was used for the dispersion interactions. The SCF cycle was converged to an electronic gradient tolerance of 1×10^{-5} by adopting the orbital transformation method.[28] The initial guess was given by the stable predictor-corrector extrapolation method at each molecular dynamics step.[40,41] The energy cut-off for the auxiliary plane-wave basis set was set to 300 Ry, and a time step of 0.5 fs was used for integrating the equations of motion. All simulations were performed at 300 K with the Nose–Hoover chain thermostat.[42,43]

For our simulations of bulk aqueous systems, we considered a single dimethylamine molecule and 64 water molecules in a cubic box with side lengths of 12.42 Å (which corresponds to the experimental density of 64 water molecules). The system was then equilibrated with classical MD simulations at 300 K to prepare initial configurations for subsequent AIMD simulations. We used the SPC/E[44] and OPLS[45] force fields for water and dimethylamine, respectively, during our classical force field simulations. A 15 ps *NPT* simulation was subsequently performed at 300 K to obtain the correct box length for a single dimethylamine molecule in water. The density was then calculated from the *NPT* simulation, and the resulting density of this mixture reached 1.025 g cm^{-3}. After setting the average box length (12.47 Å), we performed a 5 ps *NVT* simulation with a massive Nose–Hoover chain thermostat.[42,43] We created five independent configurations from the last 1 ps of the simulation, and another 20 ps of an *NVT* simulation was carried out with a global Nose–Hoover thermostat for each trajectory. Periodic boundary conditions were applied in each of the *x*, *y*, and *z* directions for simulations of these bulk aqueous systems, which is shown in Fig. 1a.

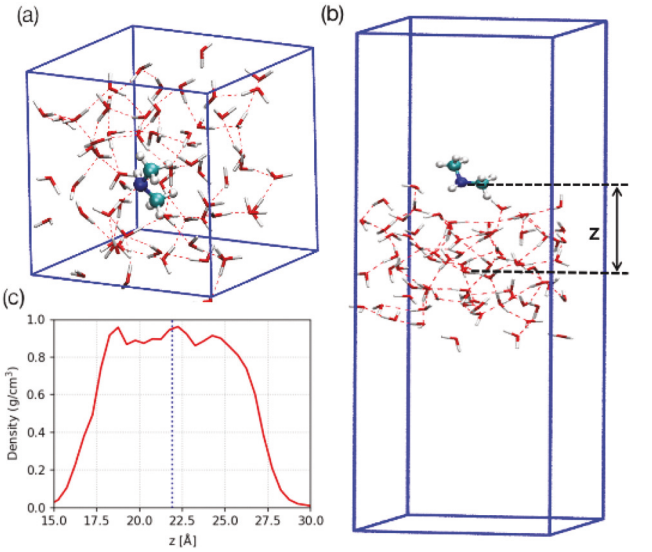

Fig. 1 Representative (a) bulk and (b) slab configurations of dimethylamine in explicit water. (c) Mass density profile of the water slab investigated in this work. The blue dashed line indicates the center of the slab.

To understand air–water interfacial effects, we generated a thin water slab comprised of 73 water molecules within a rectangular supercell with dimensions of 13.47 × 15.56 × 40 Å, shown in Fig. 1b. Slab models with similar compositions have been previously shown to provide a reasonable air–water interface for understanding surface effects.[23,24,46] Periodic boundary conditions were applied in the *x* and *y* directions of the slab. Thus, the *xy* plane of the slab system is parallel to the surface, and the *z*-axis forms the surface normal where dimethylamine interacts with the water molecules at the air–water interface. Before the addition of dimethylamine to the slab, the bare water slab was equilibrated in an *NVT* ensemble for 15 ps using a massive Nose–Hoover chain thermostat at 300 K. A density profile of the bare water slab is shown in Fig. 1c, and the density (0.9 g cm^{-3}) is approximately constant between z = 19–25 Å. As such, we observe bulk-like water behavior within this 6 Å-thick layer in the center of the slab. The calculated density profile here is very similar to the previously calculated density profile by Mundy *et al.*, which used the gradient corrected BLYP functional.[47] After equilibration, we introduced a single dimethylamine molecule at 7–12 Å above the center of mass of the slab along the *z*-direction. Similar to our calculations for bulk aqueous systems, we also created five independent initial trajectories for our slab simulations. In

these subsequent calculations, the center of mass of the dimethylamine molecule was constrained, and an additional 2 ps of *NVT* equilibration was carried out for each trajectory with the massive Nose–Hoover chain thermostat. Next, the constraint was removed, and additional *NVT* simulations (each having a duration of 25 ps) were performed for five trajectories at 300 K. We used a harmonic constraint with a spring constant value of $K = 1$ Hartree throughout the simulations to maintain the slab at the origin of the coordinate system, as suggested by previous studies.[21–24] The various structural and dynamical properties were calculated for the slab system by averaging the five independent trajectories.

2.2 Metadynamics simulations

To describe the proton transfer between dimethylamine and the surrounding water molecules, we calculated the free energy surface from metadynamics calculations.[48–51] In the metadynamics formalism, the free energy surface is generated from a biasing potential that depends on the set of predefined collective variables. In the standard metadynamics algorithm,[52,53] small repulsive biases in the form of Gaussian functions are added periodically to the potential energy to smoothly bias the system out of the energy minima. As shown in eqn (1), the metadynamics potential, $V_{\mathrm{meta}}(s,t)$, is equal to the sum of energies from these Gaussian "hills":

$$V_{\mathrm{meta}}(s,t) = \sum_{t'=\tau,2\tau,\ldots}^{t} \omega \mathrm{e}^{-V(s,t')} \exp\left[-\frac{[s-s(t')]^2}{2\sigma^2}\right]. \quad (1)$$

In eqn (1), ω is an energy rate, and σ is the width of the Gaussian of the ith CV. The energy rate, ω, is constant and is expressed in terms of the Gaussian height W and deposition rate τ as:

$$\omega = W/\tau. \quad (2)$$

As the simulation time tends toward infinity, the metadynamics potential equals the negative of the potential of the mean force plus a constant, C:

$$V(s,t \rightarrow \infty) = -F(s) + C. \quad (3)$$

The initial coordinates for our metadynamics simulations were taken from AIMD simulations for both the bulk and slab systems. The metadynamics formalism in its extended Lagrangian version was employed to explore the free-energy profile of the dissociation process using the following collective variables:[54,55] n_{OH}, the number of hydrogens coordinating the oxygen of water, and n_{NH}, the number of hydrogens coordinating the nitrogen of the amine group.

$$\mathrm{CV}_1 \text{ or } n_{\mathrm{OH}} = \frac{1-\left(\frac{r_{\mathrm{OH}_i}}{r_{\mathrm{c}}}\right)^{p}}{1-\left(\frac{r_{\mathrm{OH}_i}}{r_{\mathrm{c}}}\right)^{p+q}} \quad (4)$$

$$\mathrm{CV}_2 \text{ or } n_{\mathrm{NH}} = \frac{1-\left(\frac{r_{\mathrm{NH}_i}}{r_{\mathrm{c}}}\right)^{p}}{1-\left(\frac{r_{\mathrm{NH}_i}}{r_{\mathrm{c}}}\right)^{p+q}} \quad (5)$$

In eqn (4) and (5), p and q are constants and were both set to 6. These values were utilized to distinguish between coordinated and non-coordinated states. The use of a coordination number rather than a bond length as a CV is more robust for exploring aqueous deprotonation and proton transfer, particularly in stabilizing and better sampling short-lived states such as the contact ion pair and the solvent-separated ion pair.[56] The parameter r_{OH} is the instantaneous distance between O and H of H_2O, and r_{NH} denotes the distance between the N atom in dimethylamine and an H atom in a surrounding H_2O molecule. The parameter r_{c} in eqn (4) and (5) indicates the reference distance for OH and NH distances. For our calculations, we chose r_{c} to be 1.50 and 1.10 Å for O–H and N–H, respectively. The deposition rate for the Gaussian hills was 10 MD steps, which allows each Gaussian hill to be spawned every 5 fs. It should be noted that for systems characterized by a high reactivity (such as ultrafast proton transfer from water to anions on a femtosecond time scale,[57–59] aqueous proton conduction across two-dimensional graphyne,[60] or irreversible reactions[61]), a Gaussian hill deposition rate of every 10 MD steps is a common and sufficient choice.[62,63] However, in numerous instances, such as force-field based metadynamics simulations of alanine dipeptide or tri-peptide in vacuum,[64] dissociation of weak acids from AIMD simulations,[24] and systems having activation barriers (where several picoseconds of metadynamics simulation time are required[65]), several hundred steps are used for the Gaussian hill deposition. In the present case, proton transfer occurs within a femtosecond time scale due to its high reactivity and, therefore, 10 MD steps for Gaussian hill deposition was used in our simulations. We also performed standard metadynamics calculations with a 10 fs Gaussian hill deposition rate to check the convergence of the free energy profile. The height and width of the Gaussian hill to spawn was set to 10^{-3} Hartree and 0.03 a.u., respectively. The atomic mass unit and λ parameter for both collective variables in the extended Lagrangian scheme were set to 10 and 0.1, respectively. A scaling factor of 0.08, which determines the amplitude of the Gaussian of the CVs, was adopted for both collective variables. The free energy was obtained from the biasing potential being added at time t in the collective variable space s. We have carried out three metadynamics calculations using different initial conditions for the bulk aqueous and air–water interface environments. Our standard metadynamics calculations suggest that proton transfer occurred within a few hundred femtoseconds. Therefore, to obtain a metadynamics trajectory with a longer duration, we also employed well-tempered metadynamics simulations,[66] which has been shown to converge asymptotically.[67] Our well-tempered metadynamics simulations were carried out with ΔT = 600 K and ran for 7–13 ps (which provides extensive sampling and convergence) for both the bulk aqueous environment and the air–water interface.

3 Results and discussion

3.1 Surface preference

To further explore properties of our air–water interface model, we calculated the vertical distance between the center of mass

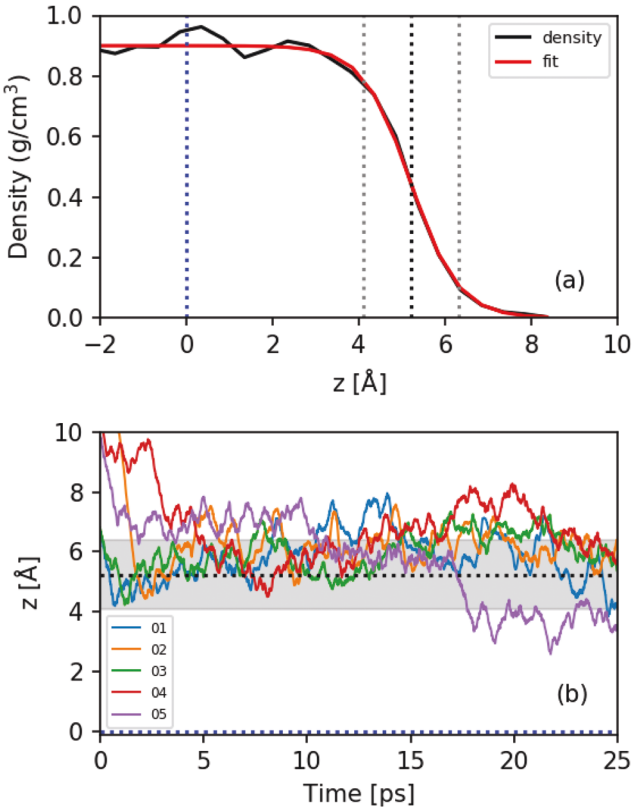

Fig. 2 (a) Fitted density profile of the water slab. The vertical black dotted line indicates the position of z_{GDS}, and grey dotted lines indicate the interfacial thickness, $z_{GDS} \pm \delta$. (b) Distance between the center of mass of the slab and the N atom of dimethylamine. The Gibbs dividing surface is denoted by the horizontal black dotted line, and the grey area is the interfacial thickness within $\pm\delta$ of the slab. The dotted blue lines in both panels indicate the center of the slab, which is set to zero in our calculations.

of the water slab and the nitrogen atom of dimethylamine as a function of time. The computed results for five trajectories are shown in Fig. 2b. The black dashed horizontal line at 5.21 Å denotes the air–water interface position (*i.e.*, the Gibbs dividing surface) from the center of mass of the slab. The Gibbs dividing surface was determined by fitting the density profile to the following hyperbolic tangent function:

$$\rho(z) = \frac{1}{2}(\rho_l + \rho_v) - \frac{1}{2}(\rho_l - \rho_v)\tanh\left(\frac{z - z_{GDS}}{\delta}\right), \qquad (6)$$

where ρ_v is the density of the vapor phase (set to 0 g cm^{-3}), and ρ_l is the density of the water liquid phase; z_{GDS} is the position of the Gibbs dividing surface (the point where the density is half the bulk water density), and δ is the interfacial width. Upon fitting to this functional form, we obtained the following values: ρ_l = 0.91 g cm^{-3}, z_{GDS} = 5.21 Å, and δ = 1.1 Å. The fitted density profile of the slab is shown in Fig. 2a. Thus, the top surface of the water slab where the dimethylamine will collide is indicated by the $z_{GDS} - \delta < z < z_{GDS} + \delta$ region.

Fig. 2b shows our results in which a dimethylamine molecule was placed at different heights from the center of the slab. We define our interface to be the $z_{GDS} - \delta < z < z_{GDS} + \delta$ region within the water slab, and all trajectories in Fig. 2b show that the dimethylamine becomes localized in this region after 2 to 4 ps. Due to limitations associated with the computationally intensive *ab initio* simulation, diffusion into the bulk was not observed, except for only one trajectory (labeled as 05), which shows this effect during a 25 ps simulation period. As such, the dimethylamine molecule remains primarily near the air–water interface throughout most of our simulations.

3.2 Radial distribution functions

The radial distribution function (RDF) captures critical structural features that describe interactions between dimethylamine and water. In Fig. 3, we plot the RDF between the N atom of dimethylamine and the H atom of water (H_w) for bulk *vs.* slab environments. The N–H_w RDFs for five trajectories (labeled as 01, 02, 03, 04, and 05) in a bulk aqueous environment are shown in Fig. 3a. The number integral (NI) represents the coordination number. The sharp peaks at 1.10 Å followed by the minima at 1.30 Å for trajectories 01 and 04 indicate the formation of an N–H bond. The NI values up to the first minima positions (1.30 Å) for trajectories 01 and 04 are approximately one, which suggests that about one proton is transferred from a neighboring water molecule to the N atom of dimethylamine. A small peak can be seen for the other trajectories at 1.10 Å, which shows a partial proton transferred from water to dimethylamine. Additional secondary peaks can be found near 1.70 Å, followed by deeper minima at 2.50 Å for all the trajectories in the bulk configuration.

The integration of the second peaks up to the second minima positions leads to a hydration number of 1.0. These peaks are associated with the hydrogen bond formation

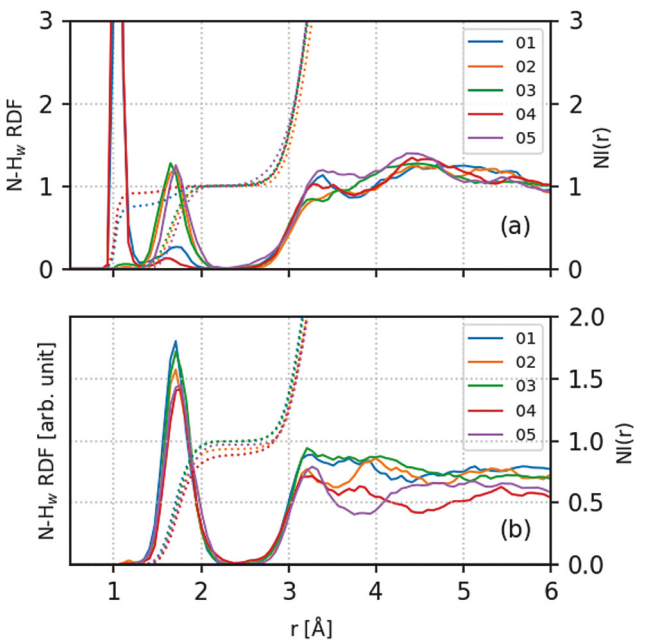

Fig. 3 (a) Radial distribution functions (RDFs) for the N–H_w pair in a bulk aqueous environment. (b) RDF for the N–H_w pair in a slab configuration. In both panels, the solid line indicates the RDF, and the dashed line indicates the number integral (NI).

between the N atom of dimethylamine and the H atom of surrounding water molecules. Therefore, the N atom of dimethylamine participates in approximately one hydrogen bond formation in a bulk aqueous environment.

The N–H_w RDFs for the slab configuration are displayed in Fig. 3b for all the trajectories. The RDF units are arbitrary since the box lengths in the *x*, *y*, and *z*-directions are different. Therefore, we used a relative unit of measurement to indicate the relative atom distribution as a function of the distance between the N atom of dimethylamine and the H atoms of the surrounding water molecules for the slab. A very tiny peak is observed at 1.10 Å for the N–H_w RDFs for the slab configuration, which might signify a partial proton transfer. Sharp peaks can also be seen at 1.70 Å, which is accompanied by subsequent minima at 2.50 Å. For the slab configuration, integration of the peaks up to the first minima contributes to approximately one hydrogen bond coordination for the N atom of dimethylamine. Overall, dimethylamine makes about one hydrogen bond with the surrounding water molecules in both the bulk and air–water interface environments.

The N–H moiety in dimethylamine can act as a hydrogen bond donor. To probe this hydrogen–bonding interaction, we also calculated H–O_w RDFs (where O_w denotes an O atom of water) in both bulk and slab environments, which are shown in Fig. 4. The H–O_w RDF pair gives the first peak at 1.81 Å, followed by a minimum at 2.05 Å (Fig. 4a). The first peak position indicates the formation of a hydrogen bond. A shallow minimum in the H–O_w RDF indicates a weak hydrogen bond forms between the aminic hydrogen and the surrounding water molecules, which contrasts with the N–H_w RDF for a bulk aqueous environment, shown previously in Fig. 3a. The value of the number integral (NI) up to the first minimum is 0.40, which corresponds to the hydrogen-bond number. In Fig. 4b, we plot the H–O_w RDF for the slab configuration. The first peak is located at 2.20 Å, which is slightly larger than the first peak in the H–O_w RDF in a bulk aqueous environment. This observation implies that the aminic hydrogen of dimethylamine makes a weaker hydrogen bond with water molecules present at the air–water interface. The integration up to the first minimum position (2.80 Å) gives a hydration number of approximately 0.55, which is slightly larger than that of the bulk configuration. Taken together, the RDF and NI calculations suggest that dimethylamine makes more effective hydrogen bonding interactions *via* the N atom compared to the aminic hydrogen.

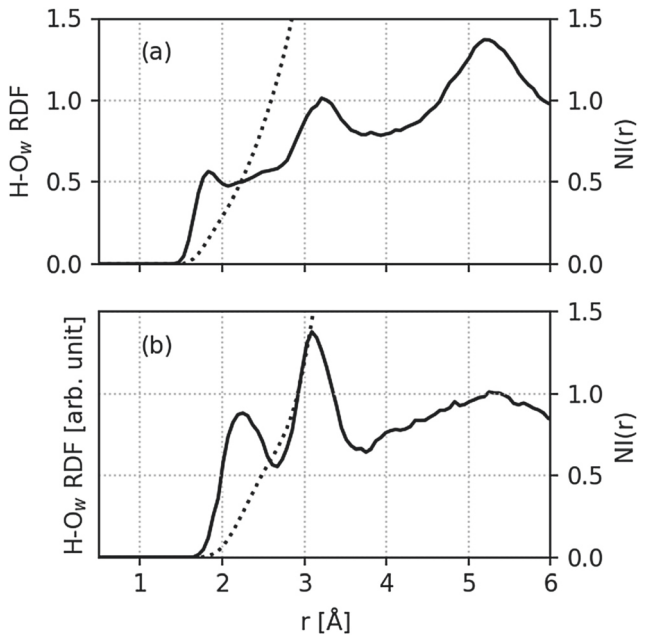

Fig. 4 (a) Radial distribution function (RDF) for the H–O_w pair in a bulk aqueous environment. Panel (b) represents the H–O_w RDF for a slab configuration. In both panels, the solid line indicates the RDF, and the dashed line indicates the number integral (NI).

3.3 Hydrogen bond dynamics

Hydrogen bonding constitutes the primary interaction between the N–H moiety of dimethylamine and the surrounding water molecules in both the bulk and slab/interfacial configurations. From the RDF calculations, we find that the N atom of dimethylamine can form more hydrogen bonds with water molecules in both the bulk and slab configurations than that of the aminic hydrogen. This observation is consistent with other RDF calculations of N–H moieties in water, such as methylamine[68] and NH_2 radical in aqueous environments.[69] To provide a deeper understanding of the strength and dynamic stability of the various hydrogen bonds, we can construct a hydrogen bond auto-correlation function using a population correlation function approach.[70–76] In this work, we construct a continuous hydrogen bond auto-correlation function that describes the probability that a particular hydrogen-bonded pair remains bonded up to a time of *t*. For hydrogen bond dynamics calculations of bulk water, Luzar and Chandler designated a hydrogen bond to occur when the O–O bond distance was $\leq$3.35 Å with a hydrogen bond cut-off angle of 30°[70, 71, 72] (taken from the RDF). Other studies have used less stringent criteria with cut-off angles of 45°[77] or only employed distance-based criteria between the N–H group and surrounding water molecules.[68,78–80] In the present study, our RDF calculations show that the dimethylamine molecule makes a single hydrogen bond with water molecules *via* the N terminal group but makes less than one hydrogen bond *via* the H atom in the N–H group with neighboring water molecules. Due to the variation in the number of hydrogen-bonds formed by dimethylamine with the surrounding water, we have only adopted a distance-based criteria to allow more flexibility in the calculation of the hydrogen-bond autocorrelation function. The geometric criteria for N–H_w and H–O_w hydrogen bonds were obtained from the corresponding radial distribution functions.

The following equation defines the time-dependent continuous hydrogen-bond auto-correlation function:

$$S_{\mathrm{HB}}(t) = \left\langle \frac{h_{ij}(0)H_{ij}(t)}{h_{ij}(0)^2} \right\rangle \quad (7)$$

In eqn (7), h_{ij} is the hydrogen bond population operator that measures the distance between *i* and *j* pairs, and the brackets signify an average of all types of hydrogen bond pairs. Our

model defines a hydrogen bond if the N–H_w distance is less than 2.50 Å (*i.e.*, the minimum position of the N–H_w RDF) for both the bulk and slab configurations. Likewise, the geometric criteria for H···O_w hydrogen-bond pairs are taken from the position of the first minima of the RDFs. The population variable, $h_{ij}(t)$, is unity when N···H_w or H···O_w is hydrogen bonded at time t and zero otherwise. Similarly, H_{ij} is equal to 1 if a hydrogen bond continuously exists from time t = 0 to t; otherwise, it is zero. The continuous auto-correlation functions for N–H_w and H–O_w hydrogen bond pairs are shown in Fig. 5.

Our results reveal that the H–O_w hydrogen bond decays faster than the N–H_w hydrogen bond correlation. Upon closer examination of the N–H_w hydrogen bond correlation in Fig. 5, we find that the decay rate at the air–water interface is slower than that in the bulk aqueous environment. This comparison also signifies that substantially more hydrogen bonding occurs at the air–water interface *via* the N atom of dimethylamine with other water molecules. The opposite trend is seen for the H–O_w hydrogen bond auto-correlation pair: at the air–water interface, the H–O_w hydrogen bond pair decays faster than that of the bulk configuration. The faster decay of the H–O_w hydrogen bond pair is due to the hydrogen atom being exposed to vacuum and less accessible towards hydrogen bond formation with the interfacial water molecules. In previous studies on the NH_2 radical,[69] (which has a similar chemical topology as dimethylamine) the nitrogen atom in the amine group interacts with water molecules predominantly at the surface, whereas one of the hydrogen atoms is left exposed to vacuum. Consequently, the H–O_w hydrogen bond at the air–water interface in this previous study also showed a shorter hydrogen bond lifetime value. In another similar system, AIMD simulations of deuterated methylamine in a bulk aqueous environment showed stronger hydrogen bonding interactions between the N atom and H_w, with the N–H_w hydrogen bonding pair correlation function decaying much slower than that of H–O_w.[68] Finally, a similar result was obtained from empirical force field simulations of methylamine in water for both bulk and interfacial environments.[81]

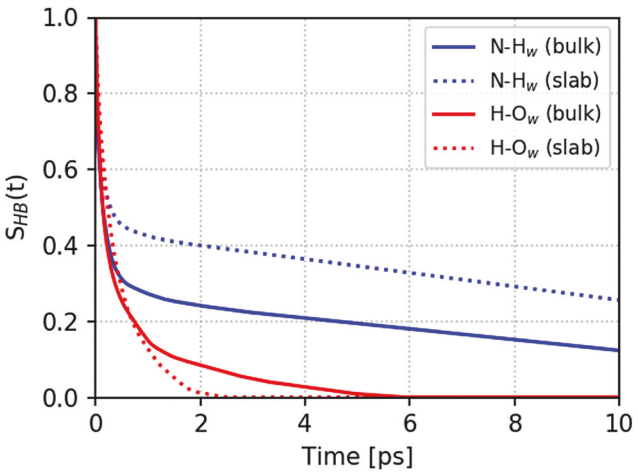

Fig. 5 Continuous hydrogen bond auto-correlation functions for N–H_w and H–O_w pairs.

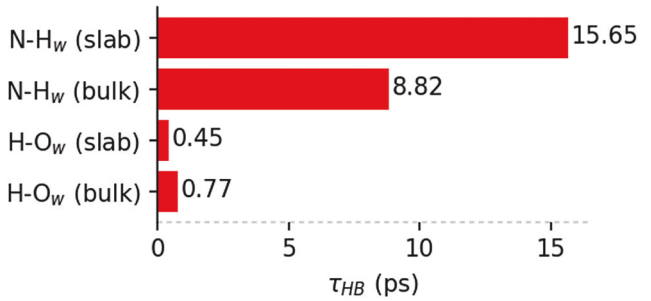

Fig. 6 Hydrogen bond lifetimes (in picoseconds) of various hydrogen bonds pairs.

In all of these cases, our calculated results for the rapid decline of the H–O_w hydrogen bond correlation compared to the N–H_w hydrogen bonding partner is consistent with previous findings on similar systems.[68,69,81]

The average hydrogen bond lifetime, τ_{HB}, can be calculated *via* the integration of eqn (7):

$$\tau_{HB} = \int_0^\infty S_{HB}(t)\mathrm{d}t. \quad (8)$$

In our work, the correlation function, $S_{HB}(t)$, was fitted to a single exponential function to calculate τ_{HB}, which is summarized in Fig. 6 for the various hydrogen bond pairs. In summary, the average number, strength, and lifetimes of the hydrogen bonds show that the interaction between dimethylamine and the surrounding water molecules is governed by the N···H_w hydrogen bond interactions in the bulk and slab configurations. We also investigated the cut-off angle's sensitivity to the hydrogen-bond dynamics of the most relevant N···H_w pair in the bulk and at the air–water interface. For our calculations, we used a hydrogen-bond cut-off angle of 30°, and our results are shown in Fig. S1 in the ESI.† Our calculations conclusively show that the N···H_w hydrogen bond auto-correlation function at the air–water interface decays slower than that in the bulk aqueous environment, regardless of whether a distance-based criteria or both a distance- and angle-based criteria are used.

3.4 Proton transfer

From the N–H_w RDF calculations, we observe sharp peaks at 1.10 Å in the bulk aqueous environment and a small peak at 1.18 Å in the slab configuration during our *NVT* simulations. These peaks indicate a proton or partial proton transfer in both of these environments.

To better understand the proton transfer process, we show snapshots of the proton transfer event in the bulk and air–water interfacial environments in Fig. 7a and b, respectively. Fig. 7a shows a snapshot where one water molecule (O1) donates a proton (H1) to the N atom, and an additional two water molecules are hydrogen-bonded to the donor water molecule (O1) in the bulk aqueous environment. Experimental gas-phase[82] and theoretical studies[57–59] suggest that this kind of arrangement is known to be a low-energy configuration and can serve as a critical cluster size for the proton transfer from water

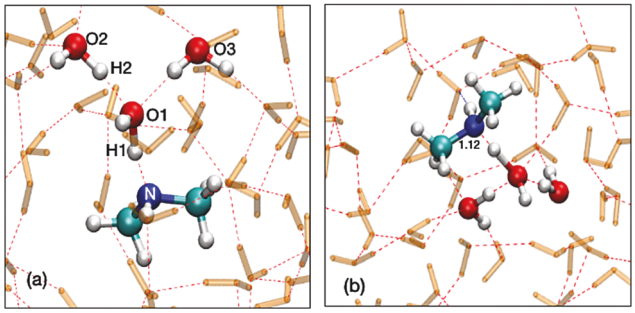

Fig. 7 (a) Snapshot before proton transfer in a bulk aqueous environment and (b) snapshot before proton transfer for trajectory 02 at the air–water interface. The water molecules that take part in the proton transfer event are shown as solid balls/bonds, whereas the rest of the spectator water molecules are depicted as orange-colored licorice sticks.

to an anion. A very similar type of configuration is also found at the air–water interface (Fig. 7b).

To further explore the proton transfer process, we calculated various bond distances as a function of time. The computed results for trajectories 01 and 04 in the bulk aqueous environment are shown in Fig. 8. Trajectories 01 and 04 depict a complete proton transfer from water to dimethylamine with different time scales, which is denoted by a black dotted line in both panels of Fig. 8. Past this point in time, the N–H1 bond distance fluctuates at around 1 to 1.10 Å, which infers that an N–H1 covalent bond formation occurs, and the H1 proton never returns to the water molecule (O1). The time scales for complete proton transfer events are 7.86 and 3.85 ps for trajectories 01 and 04, respectively, as shown in Fig. 8. Before the complete proton transfer, the N–H1 distance fluctuates between 1.10 to 1.80 Å for both trajectories, indicating a protonation and deprotonation process. The extremely fast nature of this process in both trajectories demonstrates that a concerted proton transfer process occurs *via* the simultaneous, cooperative motion of two or more protons.[24] To quantify this process, we calculated O1–H2 distances for both trajectories, and the computed results are shown in Fig. 8. For this simulation, the H2 atom is initially covalently bonded to O2 and hydrogen-bonded to a water molecule (O1), as shown in Fig. 7a. Due to their proximal distance, water molecule O2 is more prone to donate a proton (H2) to water molecule O1 compared to molecule O3. It is further seen that the O1–H2 distance shrinks to ≈1 Å at 7.86 and 3.95 ps for trajectories 01 and 04, respectively. These time scales are very similar to the proton transfer event from water (O1) to N of dimethylamine. This phenomenon indicates that when the H1 proton is completely transferred from water (O1) to the N atom, the H2 proton is simultaneously transferred to the O1 atom from the O2 atom. Thus, the proton transfer event involving H1 and H2 is approximately concerted, which has also been observed in other aqueous,[83–87] ice,[88–90] and biological systems.[91] In liquid water, the proton transfer event (*i.e.*, the Grotthuss mechanism) has been thought to be governed by sequential proton transfer events.[92–94] However, the Grotthuss mechanism in liquid water was recently re-investigated and is now considered to occur *via* a concerted mechanism in which proton migration takes place through a hydrogen bond network between closely spaced water molecules.[83] In the present case, we have also observed that proton migration happens through the hydrogen-bond network.

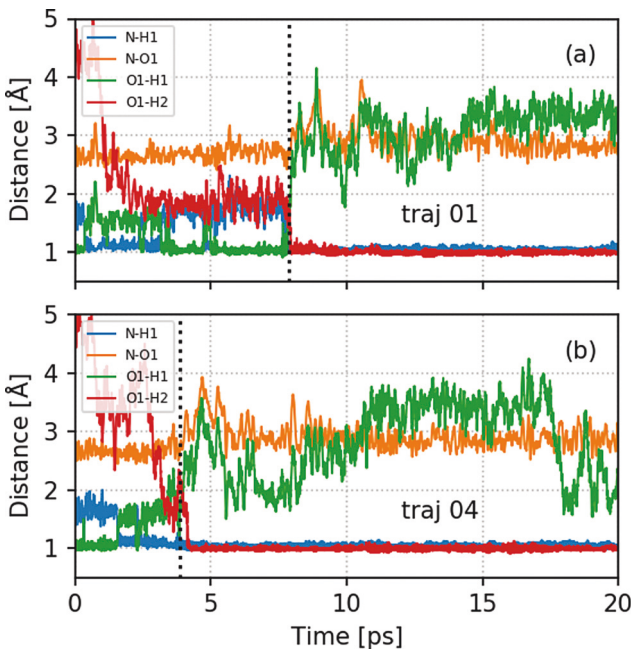

Fig. 8 Evolution of N–H1, N–O1, O1–H1, and O1–H2 distances for *NVT* simulations of trajectories 01 and 04, which describe dimethylamine protonation in a bulk aqueous environment. The corresponding atom labeling is shown in Fig. 7a. The black dotted line in both panels indicates the proton transfer event.

The metadynamics simulations in our study were performed by appropriating two collective variables (CVs). In the present calculation, we choose CV1, defined as a coordination number (CN) from O_w to H_w. The second collective variable, CV2, was selected between the N atom of dimethylamine and an H_w atom from a surrounding water molecule. Fig. 9 represents the free energy profile of the protonation of dimethylamine in a bulk aqueous environment. The states of the system can be distinguished by the CVs defined in eqn (4) and (5). The starting geometry of our metadynamics simulations was obtained from trajectory 04 from our *NVT* simulations for the bulk aqueous configuration. The reactant, *R*, is defined by the coordination numbers $n_{OH} \approx 0.9$ ($r_{OH} \approx 1.07$ Å) and $n_{NH} \approx 0.1$ ($r_{NH} \approx 1.51$ Å), in which the dimethylamine molecule is neutral or hydrogen-bonded to a water molecule. The free energy surface exhibits a deep and single-centered well that characterizes a stable reactant state. The protonated dimethylamine product, P, is defined by the coordination numbers $n_{OH} \approx 0.1$ ($r_{OH} \approx 1.65$ Å) and $n_{NH} \approx 0.8$ ($r_{NH} \approx 1.05$ Å). The transition state barrier for the protonation (labeled as TS) is located between the R and P states. The corresponding coordination numbers for CV1 and CV2 are ≈0.53 and ≈0.27, respectively. The transition state shares the proton configuration where r_{OH} is ≈1.24 Å and r_{NH} is ≈1.41 Å. The free energy activation barrier for the proton transfer from water to dimethylamine is ≈11 kJ mol^{-1}. The reactant (R),

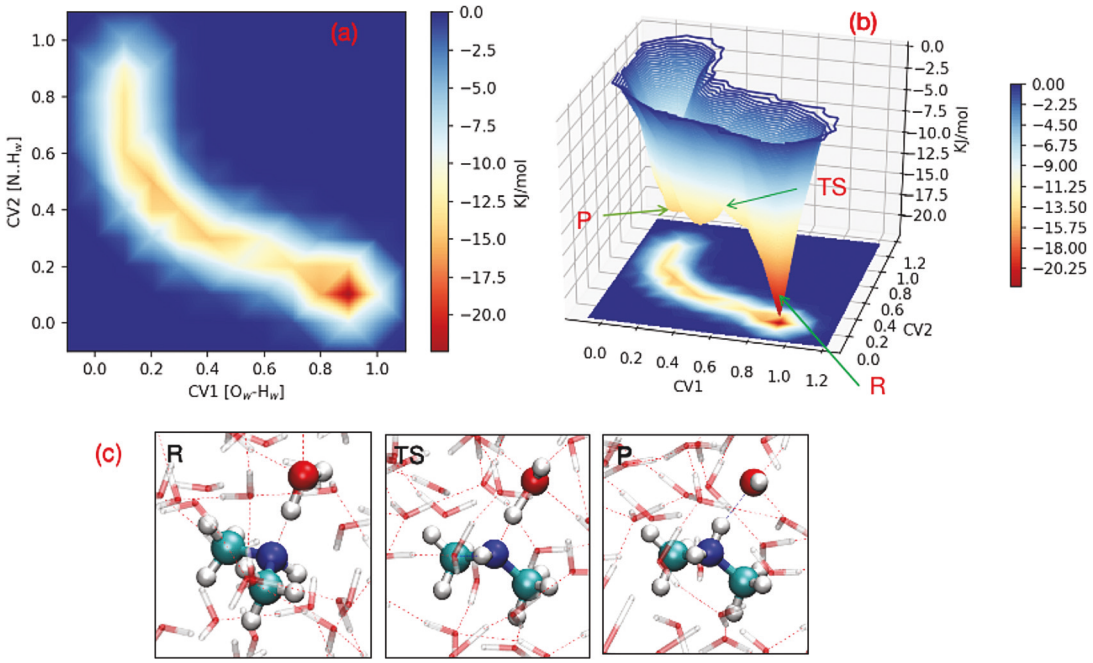

Fig. 9 Reconstructed free energy surface for the protonation of dimethylamine in a bulk aqueous environment. Panel (a) shows the 2D reconstructed free energy surface, and CV1 and CV2 represent the coordination number between O_w–H_w and N···H_w, respectively. Panel (b) represents the 3D reconstructed free energy surface, where R, TS, and P correspond to the reactant, transition state, and product. Panel (c) shows snapshots of R, TS, and P from the metadynamics simulations.

transition state (TS), and product (P) from the metadynamics simulations in the bulk aqueous environment are shown in Fig. 9c. In the ESI,† we provide two additional free energy profiles (Fig. S3 and S5 in the ESI† from trajectories 01 and 05, respectively) that utilize different initial conditions in the bulk aqueous environment. In both of these cases, the reactant proceeds towards the product *via* a stable transition state with free energy barrier values of 14.83 and 14.56 kJ mol^{-1} for trajectories 01 and 05, respectively. As such, the average free energy value from these three independent trajectories is 13.46 kJ mol^{-1}. In the ESI,† Fig. S9 depicts the fluctuation of the collective variables as a function of time for the bulk aqueous environment, which shows several forward and reverse trajectories. Our free energy barrier values are somewhat lower than those calculated for other similar systems such as the 17.57 kJ mol^{-1} activation barrier for proton transfer from water to the pyrazole anion,[57] the 27.7 kJ mol^{-1} barrier height for proton transfer from water to anilide,[59] and the 46 kJ mol^{-1} free energy barrier for the protonation of hydroxide anion between two magnesium cations in an aqueous solution.[61] However, our calculated free energy activation barriers are very close to previously reported values for the protonation of water to the ketyl radical anion, which used a similar simulation methodology.[58] We also performed convergence tests with a 10 fs hill deposition rate, and the resulting free energy profile is shown in Fig. S10 (ESI†). Based on our tests, we find that the free energy barrier decreases with increasing hill deposition rate.[60]

It should be noted that a precise evaluation of the free energy requires an average over all of the free energy profiles to sufficiently explore the entire phase space spanned by the CVs. This can be carried out by increasing the simulation time until all accessible regions of the potential are explored, with trajectories crossing forward and backward several times between the reactant to the product regions. Our various calculations of the bond distances from the non-biased simulations suggest, however, that once the proton is transferred completely from water to dimethylamine, the reverse reaction is not observed since the reaction is irreversible. In other words, when our metadynamics simulations were initiated from the stable configuration obtained from the non-biased simulations (see Computational details section), the proton transfer mechanism completed quickly within a few hundred femtoseconds. In regards to the convergence of our simulations, in the ESI,† we show that the free energy gradually builds up as a function of CV2 for both the bulk aqueous and interfacial environments. Fig. S2–S21 in the ESI† also present a detailed analysis of the free energy convergence between the transition state and product basin as well as between the product and reactant basin. Although our metadynamics simulations are short, we can still confirm a satisfactory convergence of the free energy profiles due to its high reactivity. From our convergence plots in the ESI,† the free energy barrier still converges sufficiently as the simulation time increases, despite having different initial metadynamics conditions for all the bulk and air–water interface trajectories. We would also like to point out that our selection of CVs did not significantly affect the free energy barrier value,[64] and our choice of CV was able to clearly distinguish the reactant, transition state, and product basins in all of our simulations.

The reconstructed free energy surface for the protonation of dimethylamine from the surrounding water molecules at the air–water interface is shown in Fig. 10. The initial geometry for the metadynamics simulations at the air–water interface was taken from the *NVT* simulations of trajectory 02. We have performed two additional metadynamics calculations (using different initial conditions) for the air–water interface, and the free energy profiles are shown in the ESI.† In these simulations, the protonation of dimethylamine proceeds in two substeps at the air–water interface, as shown in Fig. 10c. The coordination numbers n_{OH} ($\approx$0.92) and n_{NH} ($\approx$0.10) define the reactant state R. At this state, the dimethylamine is hydrogen-bonded to an interfacial water molecule. The typical O_w–H_w and N–H_w distances were found to be 0.99 and 1.55 Å, respectively. At the air–water interface, the deep and single-centered minimum indicates a stable reactant. Subsequently, the water molecule approaches and interacts with the N atom of dimethylamine to form a transition state in which the O_w–H_w distance is stretched to 1.11 Å (TS1). The distance from H_w to the N atom at the surface is subsequently reduced to 1.39 Å, while the O_w–H_w distance is further increased to 1.24 Å, forming a stable intermediate (I). The reaction then progresses over a second transition state where the O_w–H_w bond subsequently dissociates, and the resulting fragment binds to the surface N atom of dimethylamine. The corresponding coordination numbers for CV1 and CV2 at TS2 are $\approx$0.45 (n_{OH}), and $\approx$0.82 (n_{NH}). At TS2, the proton is shared by the oxygen and nitrogen atoms, and the corresponding O_w–H_w and N–H_w distances are 1.36 and 1.24 Å, respectively. The value of CV2 (n_{NH}) varies from $\approx$0.1 to $\approx$0.96 when a proton is completely transferred from water to dimethylamine. The product, P, is situated at $n_{OH} \approx 0.3$ ($r_{OH} \approx 1.52$ Å) and $n_{NH} \approx 0.96$ ($r_{NH} \approx 1.02$ Å). From the lowest minimum of the free energy surface, the reactant (R) goes to the lowest maximum transition state 2 (TS2) along the free-energy landscape *via* transition state 1 (TS1) and stable intermediate I, and thus separate the product (P) from reactant (R). The reactant (R), transition state 1 (TS1), intermediate (I), transition state 2 (TS2), and product (P) for the interfacial proton transfer from water to dimethylamine are shown in Fig. 10c. The net free energy barrier for this activation process is $\approx$6.5 kJ mol^{-1}.

As mentioned previously, we carried out two additional metadynamics calculations (using different initial conditions), shown in Fig. S13 and S15 in the ESI† for trajectories 05 and 04, respectively. For trajectory 05, the reactant proceeds towards the product state *via* a single transition state with a free energy barrier of 3.60 kJ mol^{-1}. The free energy surface corresponding to trajectory 04 at the air–water interface shows a similar reaction mechanism as trajectory 02. The free energy surfaces show no significant change in the reaction mechanism, other than minor differences in the position of the reactant, transition state, product, and energetic barrier heights for the conversion of dimethylamine to protonated dimethylamine. The entire reaction is accomplished in three steps that resemble the formation of TS1, the stable intermediate, and TS2. The maximum free energy barrier value from state R to P (*via* TS1, I, and TS2) is 6.30 kJ mol^{-1}, and the average free energy value (obtained from the different initial conditions) at the air–water interface is 5.47 kJ mol^{-1}. Our free energy values are similar to those calculated for other systems, such as the 8.0 kJ mol^{-1} free energy value for proton transfer from water to a TiO_2 surface,[95]

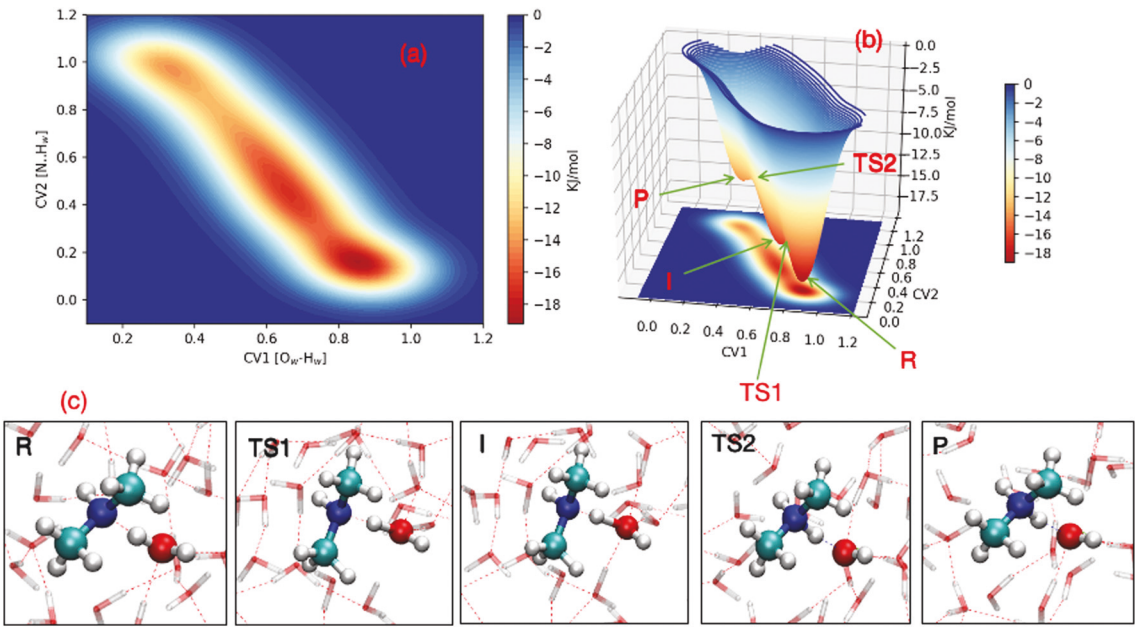

Fig. 10 Reconstructed free energy surface for the protonation of dimethylamine at the air–water interface. Panel (a) shows the 2D reconstructed free energy surface, and CV1 and CV2 represent the coordination number between O_w–H_w and N$\cdots$$H_w$, respectively. Panel (b) represents the 3D reconstructed free energy surface, where R, TS1, I, TS2, and P correspond to the reactant, transition state 1, intermediate, transition state 2, and product. Panel (c) shows snapshots of R, TS1, I, TS2, and P from the metadynamics simulations.

the 6.754 kJ mol^{-1} free energy barrier for proton transfer from liquid water film to a ZnO surface,[96] the 5.021 kJ mol^{-1} free energy barrier for proton transfer to an air–water interface in the presence of Cl^-,[97] and the 7.5 kJ mol^{-1} free energy barrier for the deprotonation of formic acid at the air–water interface computed with DFT-based metadynamics simulations.[24] The dynamical trends in the CVs for the air–water interface are depicted in Fig. S19 (ESI†), which shows several forward and reverse trajectories. In addition, the free energy profile for the air–water interface obtained with a 10 fs hill deposition rate is depicted in Fig. S20 (ESI†), which shows a decrease in the free energy barrier.

Fig. 11(a) shows the free energy surface (labeled with reactant, product, and transition state positions) for proton transfer in the bulk aqueous environment as obtained from our well-tempered metadynamics simulations. Based on the converged free energy profile, we obtain a free energy barrier of 18.40 kJ mol^{-1} with a free energy difference of 16.35 kJ mol^{-1} between the product and reactant. The free energy barrier value obtained from our well-tempered metadynamics simulation is very close to that obtained with one of our standard metadynamics calculations. Fig. 11(b) summarizes the free energy landscape for dimethylamine protonation at the air–water interface obtained with our well-tempered metadynamics simulations. The computed free energy barrier for this configuration is 12.97 kJ mol^{-1}, and the free energy difference between the product and reactant is 9.93 kJ mol^{-1}. The lower free energy value from our well-tempered metadynamics simulations at the air–water interface indicates that dimethylamine protonates faster at the interface than in the bulk aqueous environment. The dynamical trends in the CVs for the bulk aqueous environment and air–water interface from our well-tempered metadynamics simulation are shown in Fig. S22 and S23 in the ESI.† Similar to our previous calculations, the oscillations in the CVs indicate several forward and reverse crossings between the reactant and product regions.

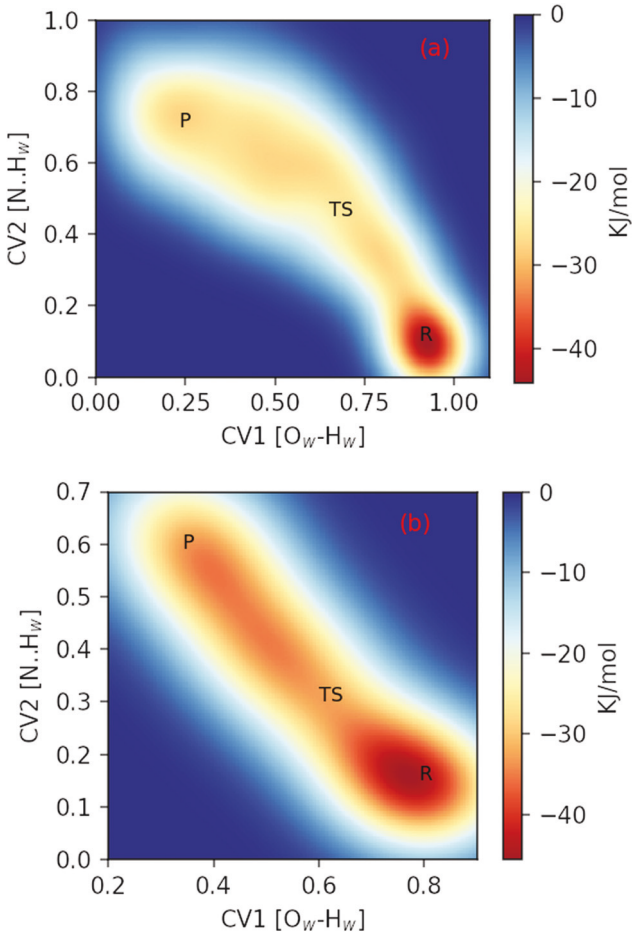

Fig. 11 Free energy surface obtained with well-tempered metadynamics simulations. Panel (a) shows the reconstructed free energy surface for the protonation of dimethylamine in a bulk aqueous environment. Panel (b) represents the reconstructed free-energy surface for the protonation of dimethylamine at the air–water interface. In both panels, R, TS, and P indicate the reactant, transition state, and product, respectively.

From the *NVT* trajectories, we observe proton transfer from water to dimethylamine in the bulk aqueous environment, and partial proton transfer at the air–water interface. However, when the dimension of the system in the bulk and slab configurations is extended by adding additional CVs (with the biasing potentials being added to the CVs directly), a lower free energy value for the slab configuration was obtained compared to the bulk aqueous environment. Our pK_b values were obtained using the equation pK_b = $\Delta G/(2.303RT)$, where ΔG is the free energy difference between the product and reactant. The pK_b values for dimethylamine from the free energy profiles obtained from trajectories 04, 01, and 05 are 1.42, 1.92, and 2.30, respectively, in the bulk aqueous environment. Therefore, the average pK_b value for dimethylamine from all of these free-energy profiles is 1.88, and the experimentally determined value is 3.28.[98] The calculated pK_b value obtained from our well-tempered metadynamics simulations for the bulk aqueous environment is 2.84. The values of the surface pK_b for dimethylamine from the free-energy profiles of trajectory 02 and 04 are 0.88 and 0.60, respectively. However, we did not calculate the pK_b value from trajectory 05, since the free energy difference between the product and reactant is very small. The average value of the surface pK_b for dimethylamine estimated from all these free-energy profiles is 0.74. We obtain a pK_b value of 1.72 at the air–water interface from our well-tempered metadynamics simulations. To the best of our knowledge, an experimental measurement of the surface pK_b value of dimethylamine at the air–water interface is not available; however, soft-X-ray and surface-sensitive photoelectron spectroscopy measurements have been used to measure the pK_b value of monoethanolamine-carbamate in aqueous environments.[99]

A small free energy barrier for the slab configuration shows that dimethylamine protonates faster than in a bulk aqueous environment. Detailed calculations of the solvation shell structure and hydrogen-bonding of the N atom of dimethylamine at the air–water interface compared to the bulk configuration are inconclusive since approximately one hydrogen bond is formed by the N atom in the bulk aqueous environment and at the air–water interface. In previous studies, the protonation of dimethylamine at the air–water interface may be due to faster

water re-orientational and hydrogen-bond dynamics,[24] or a more acidic nature of the water surface. Other *ab initio* and classical molecular dynamics simulations have shown that the water surface is acidic with a pH < 4.8.[100] Another experimental study measured the acidity of the water surface by collisions of trimethylamine (which is chemically similar to dimethylamine) on aqueous microjets.[101] Most notably, this prior study showed that trimethylamine protonates at the air–water interface when the pH value is approximately 3.8. Francisco and co-workers also reported that the pK_a value and redox potential at the air–water interface differ from the bulk aqueous environment, and the air–water interface provides an energetically favorable environment for redox reactions.[102–105] Collectively, these prior studies demonstrate that the enhancement of the surface acidity of water could be one of the reasons for the small free energy barrier for the protonation of dimethylamine, which also corroborates the results of our metadynamics simulations.

To make contact with experimental observables, we also calculated the pK_b values for the protonation of dimethylamine in bulk water and at the air–water interface. Our estimation of pK_b was carried out from the difference in free-energy values between the protonated and unprotonated states using the equation $pK_b = \Delta G/(2.303RT)$. To this end, we obtained pK_b values of 1.88 (standard metadynamics) and 2.84 (well-tempered metadynamics) for dimethylamine in the bulk aqueous environment (the experimental value is 3.28 [98]). In contrast, the surface pK_b values for dimethylamine estimated from the free-energy profiles are 0.74 (standard metadynamics) and 1.72 (well-tempered metadynamics). It should be noted that several factors are responsible for the inaccurate estimates of the absolute free energy values obtained from our AIMD-metadynamics simulation. These include the specific exchange–correlation functional used to calculate the energies/forces in these simulations and errors intrinsically associated with the metadynamics sampling technique itself. Nevertheless, we expect the overall trends of these values to be correct, with surface pK_b values lower than their bulk water configurations.

4 Conclusions

We have carried out extensive *ab initio* molecular dynamics simulations of dimethylamine to understand and contrast dynamical effects in a bulk aqueous environment *vs.* the air–water interface. Our calculations suggest that dimethylamine is strongly surface-active and remains near the air–water interface. Furthermore, our hydrogen-bonding network analysis indicates that compared to the $NH\cdots OH_2$ hydrogen-bond, the $HOH\cdots NH_2$ hydrogen bond is the dominant interaction between dimethylamine and individual water molecules. Our calculations also suggest that the $HOH\cdots NH_2$ hydrogen-bond is more robust and stronger at the air–water interface. Moreover, we find that protonation happens in only two out of five *NVT* trajectories in the bulk aqueous environment. In contrast, we observe a partial proton transfer during our *NVT* simulations at the air–water interface. In all of our calculations, the proton position fluctuates for several picoseconds before it is completely transferred *via* the hydrogen bonds connecting the donor (water) and acceptor (dimethylamine) but resides primarily on the donor water molecule. Most notably, we found that two protons were required to initiate the process for a complete proton transfer event. As such, the proton transfer from water to dimethylamine suggests a sequential and concerted proton transfer mechanism.

Our calculations provide an atomistic-level picture of the reaction path and the associated energetic aspects of the protonation process in both bulk and air–water interfacial environments. Using *ab initio*-based metadynamics to predict the free energy profile of the protonation process, we have shown that the surface pK_b of dimethylamine is lower than its bulk value. In particular, our atomistic simulations show that proton transfer from water to dimethylamine occurs more easily on an aqueous surface (or in a water cluster) than in a bulk water environment. This study provides additional mechanistic insight into the acid–base reactions involved in NPF and provides some justification for the hypothesis that the increased surface area-to-volume ratio of nanoparticles plays a role in the observed differences in size-resolved composition.[106–109]

Conflicts of interest

There are no conflicts to declare.

Acknowledgements

N. M. and J. N. S. acknowledge funding from the U.S. National Science Foundation under Grant No. CHE-1710580. S. B. H. K., K. C. B., and B. M. W. acknowledge funding from the U.S. National Science Foundation under Grant No. CHE-1710691. The *ab initio* metadynamics and enhanced sampling calculations were supported by the U.S. National Science Foundation under Grant No. CHE-1808242.

Notes and references

1 O. Boucher, D. Randall, P. Artaxo, C. Bretherton, G. Feingold, P. Forster, V.-M. Kerminen, Y. Kondo, H. Liao, U. Lohmann, P. Rasch, S. K. Satheesh, S. Sherwood, B. Stevens and X. Y. Zhang, in *Clouds and aerosols*, ed. T. F. Stocker, D. Qin, G.-K. Plattner, M. Tignor, S. K. Allen, J. Doschung, A. Nauels, Y. Xia, V. Bex and P. M. Midgley, Cambridge University Press, Cambridge, UK, 2013, pp. 571–657.
2 J. Merikanto, D. V. Spracklen, G. W. Mann, S. J. Pickering and K. S. Carslaw, *Atmos. Chem. Phys.*, 2009, **9**, 8601–8616.
3 J. Kazil, P. Stier, K. Zhang, J. Quaas, S. Kinne, D. O'Donnell, S. Rast, M. Esch, S. Ferrachat, U. Lohmann and J. Feichter, *Atmos. Chem. Phys.*, 2010, **10**, 10733–10752.
4 A. Jefferson, F. Eisele, P. Ziemann, R. Weber, J. Marti and P. H. McMurry, *J. Geophys. Res.: Atmos.*, 1997, **102**, 19021–19028.
5 V. Fiedler, M. Dal Maso, M. Boy, H. Aufmhoff, J. Hoffmann, T. Schuck, W. Birmili, F. Arnold and M. Kulmala, *Atmos. Chem. Phys.*, 2005, **5**, 1773–1785.

6 J. Kirkby, J. Curtius, J. Almeida, E. Dunne, J. Duplissy, S. Ehrhart, A. Franchin, S. Gagné, L. Ickes and A. Kürten, *et al.*, *Nature*, 2011, **476**, 429–433.
7 N. Myllys, T. Ponkkonen, M. Passananti, J. Elm, H. Vehkamäki and T. Olenius, *J. Phys. Chem. A*, 2018, **122**, 4717–4729.
8 T. Kurtén, V. Loukonen, H. Vehkamäki and M. Kulmala, *Atmos. Chem. Phys.*, 2008, **8**, 4095–4103.
9 K. C. Barsanti, P. H. McMurry and J. N. Smith, *Atmos. Chem. Phys.*, 2009, **9**, 2949–2957.
10 N. Myllys, S. Chee, T. Olenius, M. Lawler and J. N. Smith, *J. Phys. Chem. A*, 2019, **123**, 2420–2425.
11 V. Loukonen, T. Kurtén, I. K. Ortega, H. Vehkamäki, A. A. H. Pádua, K. Sellegri and M. Kulmala, *Atmos. Chem. Phys.*, 2010, **10**, 4961–4974.
12 A. Kürten, C. Li, F. Bianchi, J. Curtius, A. Dias, N. M. Donahue, J. Duplissy, R. C. Flagan, J. Hakala and T. Jokinen, *et al.*, *Atmos. Chem. Phys.*, 2018, **18**, 845–863.
13 C. N. Jen, P. H. McMurry and D. R. Hanson, *J. Geophys. Res.: Atmos.*, 2014, **119**, 7502–7514.
14 J. W. DePalma, B. R. Bzdek, D. J. Doren and M. V. Johnston, *J. Phys. Chem. A*, 2012, **116**, 1030–1040.
15 J. N. Smith, K. C. Barsanti, H. R. Friedli, M. Ehn, M. Kulmala, D. R. Collins, J. H. Scheckman, B. J. Williams and P. H. McMurry, *Proc. Natl. Acad. Sci. U. S. A.*, 2010, **107**, 6634–6639.
16 C. Qiu and R. Zhang, *Phys. Chem. Chem. Phys.*, 2013, **15**, 5738–5752.
17 N. Myllys, J. Kubečka, V. Besel, D. Alfaouri, T. Olenius, J. N. Smith and M. Passananti, *Atmos. Chem. Phys.*, 2019, **19**, 9753–9768.
18 J. Elm, *J. Phys. Chem. A*, 2017, **121**, 8288–8295.
19 J. Almeida, S. Schobesberger, A. Kürten, I. K. Ortega, O. Kupiainen-Määttä, A. P. Praplan, A. Adamov, A. Amorim, F. Bianchi and M. Breitenlechner, *et al.*, *Nature*, 2013, **502**, 359–363.
20 M. J. Lawler, P. M. Winkler, J. Kim, L. Ahlm, J. Tröstl, A. P. Praplan, S. Schobesberger, A. Kürten, J. Kirkby, F. Bianchi, J. Duplissy, A. Hansel, T. Jokinen, H. Keskinen, K. Lehtipalo, M. Leiminger, T. Petäjä, M. Rissanen, L. Rondo, M. Simon, M. Sipilä, C. Williamson, D. Wimmer, I. Riipinen, A. Virtanen and J. N. Smith, *Atmos. Chem. Phys.*, 2016, **16**, 13601–13618.
21 L. Partanen, G. Murdachaew, R. B. Gerber and L. Halonen, *Phys. Chem. Chem. Phys.*, 2016, **18**, 13432–13442.
22 I.-F. W. Kuo, C. J. Mundy, B. L. Eggimann, M. J. McGrath, J. I. Siepmann, B. Chen, J. Vieceli and D. J. Tobias, *J. Phys. Chem. B*, 2006, **110**, 3738–3746.
23 G. Murdachaew, C. J. Mundy, G. K. Schenter, T. Laino and J. Hutter, *J. Phys. Chem. A*, 2011, **115**, 6046–6053.
24 G. Murdachaew, G. M. Nathanson, R. B. Gerber and L. Halonen, *Phys. Chem. Chem. Phys.*, 2016, **18**, 29756–29770.
25 A. A. Hassanali, J. Cuny, V. Verdolino and M. Parrinello, *Philos. Trans. R. Soc., A*, 2014, **372**, 20120482.
26 A. Laio and M. Parrinello, *Proc. Natl. Acad. Sci. U. S. A.*, 2002, **99**, 12562–12566.
27 J. VandeVondele, M. Krack, F. Mohamed, M. Parrinello, T. Chassaing and J. Hutter, *Comput. Phys. Commun.*, 2005, **167**, 103–128.
28 J. VandeVondele and J. Hutter, *J. Chem. Phys.*, 2003, **118**, 4365–4369.
29 M. Krack and M. Parrinello, *Phys. Chem. Chem. Phys.*, 2000, **2**, 2105–2112.
30 J. Hutter, M. Iannuzzi, F. Schiffmann and J. VandeVondele, *Wiley Interdiscip. Rev.: Comput. Mol. Sci.*, 2014, **4**, 15–25.
31 https://www.cp2k.org.
32 G. Lippert, J. Hutter and M. Parrinello, *Mol. Phys.*, 1997, **92**, 477–488.
33 C. Hartwigsen, S. Goedecker and J. Hutter, *Phys. Rev. B: Condens. Matter Mater. Phys.*, 1998, **58**, 3641–3662.
34 S. Goedecker, M. Teter and J. Hutter, *Phys. Rev. B: Condens. Matter Mater. Phys.*, 1996, **54**, 1703–1710.
35 A. Schäfer, C. Huber and R. Ahlrichs, *J. Chem. Phys.*, 1994, **100**, 5829–5835.
36 A. D. Becke, *Phys. Rev. A: At., Mol., Opt. Phys.*, 1988, **38**, 3098–3100.
37 A. D. Becke, *J. Chem. Phys.*, 1993, **98**, 5648–5652.
38 C. Lee, W. Yang and R. G. Parr, *Phys. Rev. B: Condens. Matter Mater. Phys.*, 1988, **37**, 785–789.
39 S. Grimme, *J. Comput. Chem.*, 2006, **27**, 1787–1799.
40 J. Kolafa, *J. Comput. Chem.*, 2004, **25**, 335–342.
41 T. D. Kühne, M. Krack, F. R. Mohamed and M. Parrinello, *Phys. Rev. Lett.*, 2007, **98**, 066401.
42 S. Nosé, *J. Chem. Phys.*, 1984, **81**, 511–519.
43 W. G. Hoover, *Phys. Rev. A: At., Mol., Opt. Phys.*, 1985, **31**, 1695–1697.
44 H. J. C. Berendsen, J. R. Grigera and T. P. Straatsma, *J. Phys. Chem.*, 1987, **91**, 6269–6271.
45 W. L. Jorgensen, D. S. Maxwell and J. Tirado-Rives, *J. Am. Chem. Soc.*, 1996, **118**, 11225–11236.
46 A. D. Hammerich, B. J. Finlayson-Pitts and R. B. Gerber, *Phys. Chem. Chem. Phys.*, 2015, **17**, 19360–19370.
47 I.-F. W. Kuo and C. J. Mundy, *Science*, 2004, **303**, 658–660.
48 A. Laio and M. Parrinello, *Proc. Natl. Acad. Sci. U. S. A.*, 2002, **99**, 12562–12566.
49 M. Iannuzzi, A. Laio and M. Parrinello, *Phys. Rev. Lett.*, 2003, **90**, 238302.
50 B. Ensing, A. Laio, F. L. Gervasio, M. Parrinello and M. L. Klein, *J. Am. Chem. Soc.*, 2004, **126**, 9492–9493.
51 E. Schreiner, N. N. Nair and D. Marx, *J. Am. Chem. Soc.*, 2009, **131**, 13668–13675.
52 B. Ensing, M. De Vivo, Z. Liu, P. Moore and M. L. Klein, *Acc. Chem. Res.*, 2006, **39**, 73–81.
53 A. Barducci, M. Bonomi and M. Parrinello, *Wiley Interdiscip. Rev.: Comput. Mol. Sci.*, 2011, **1**, 826–843.
54 A. Laio and F. L. Gervasio, *Rep. Prog. Phys.*, 2008, **71**, 126601.
55 N. N. Nair, E. Schreiner and D. Marx, *J. Am. Chem. Soc.*, 2008, **130**, 14148–14160.
56 M. Sprik, *Chem. Phys.*, 2000, **258**, 139–150.
57 S. Biswas and B. S. Mallik, *Phys. Chem. Chem. Phys.*, 2016, **18**, 29979–29986.
58 S. Biswas, T. Dasgupta and B. S. Mallik, *Chem. Phys.*, 2016, **477**, 46–51.
59 S. Biswas and B. S. Mallik, *J. Mol. Liq.*, 2016, **219**, 810–814.

60 L. Shi, A. Xu, D. Pan and T. Zhao, *Nat. Commun.*, 2019, **10**, 1165.
61 J. M. Park and M. Boero, *J. Phys. Chem. B*, 2010, **114**, 11102–11109.
62 M. Heshmat, *J. Phys. Chem. C*, 2020, **124**, 10951–10960.
63 M. Ghoussoub, S. Yadav, K. K. Ghuman, G. A. Ozin and C. V. Singh, *ACS Catal.*, 2016, **6**, 7109–7117.
64 M. Invernizzi and M. Parrinello, *J. Phys. Chem. Lett.*, 2020, **11**, 2731–2736.
65 A. Ishikawa and Y. Tateyama, *J. Phys. Chem. C*, 2020, **124**, 6054–6062.
66 A. Barducci, G. Bussi and M. Parrinello, *Phys. Rev. Lett.*, 2008, **100**, 020603.
67 J. F. Dama, M. Parrinello and G. A. Voth, *Phys. Rev. Lett.*, 2014, **112**, 240602.
68 S. Biswas and B. S. Mallik, *ChemistrySelect*, 2017, **2**, 74–83.
69 J. Zhong, Y. Zhao, L. Li, H. Li, J. S. Francisco and X. C. Zeng, *J. Am. Chem. Soc.*, 2015, **137**, 12070–12078.
70 A. Luzar and D. Chandler, *Nature*, 1996, **379**, 55–57.
71 A. Luzar and D. Chandler, *Phys. Rev. Lett.*, 1996, **76**, 928–931.
72 A. Luzar, *J. Chem. Phys.*, 2000, **113**, 10663–10675.
73 A. Chandra, *Phys. Rev. Lett.*, 2000, **85**, 768–771.
74 S. Balasubramanian, S. Pal and B. Bagchi, *Phys. Rev. Lett.*, 2002, **89**, 115505.
75 H. Xu and B. J. Berne, *J. Phys. Chem. B*, 2001, **105**, 11929–11932.
76 H. Xu, H. A. Stern and B. J. Berne, *J. Phys. Chem. B*, 2002, **106**, 2054–2060.
77 S. K. Pattanayak, P. Chettiyankandy and S. Chowdhuri, *Mol. Phys.*, 2014, **112**, 2906–2919.
78 S. Biswas and B. S. Mallik, *J. Mol. Liq.*, 2020, **301**, 112395.
79 S. Biswas and B. S. Mallik, *J. Mol. Liq.*, 2015, **212**, 941–946.
80 S. Biswas and B. S. Mallik, *Phys. Chem. Chem. Phys.*, 2017, **19**, 9912–9922.
81 R. D. Hoehn, M. A. Carignano, S. Kais, C. Zhu, J. Zhong, X. C. Zeng, J. S. Francisco and I. Gladich, *J. Chem. Phys.*, 2016, **144**, 214701.
82 I. Wolf, A. Shapira, R. Giniger, Y. Miller, R. Gerber and O. Cheshnovsky, *Angew. Chem., Int. Ed.*, 2008, **47**, 6272–6274.
83 A. Hassanali, F. Giberti, J. Cuny, T. D. Kühne and M. Parrinello, *Proc. Natl. Acad. Sci. U. S. A.*, 2013, **110**, 13723–13728.
84 M. J. Cox, R. L. A. Timmer, H. J. Bakker, S. Park and N. Agmon, *J. Phys. Chem. A*, 2009, **113**, 6599–6606.
85 B. J. Siwick and H. J. Bakker, *J. Am. Chem. Soc.*, 2007, **129**, 13412–13420.
86 S. Miura, M. E. Tuckerman and M. L. Klein, *J. Chem. Phys.*, 1998, **109**, 5290–5299.
87 J. Kohanoff, S. Koval, D. A. Estrin, D. Laria and Y. Abashkin, *J. Chem. Phys.*, 2000, **112**, 9498–9508.
88 C. Drechsel-Grau and D. Marx, *Phys. Rev. Lett.*, 2014, **112**, 148302.
89 X. Meng, X. Meng, J. Peng, J. Chen, Z. Wang, J.-R. Shi, X.-Z. Li, X.-Z. Li and X.-Z. Li, *Nat. Phys.*, 2015, 235–239.
90 C. Drechsel-Grau and D. Marx, *Nat. Phys.*, 2015, 216–218.
91 V. R. I. Kaila and G. Hummer, *Phys. Chem. Chem. Phys.*, 2011, **13**, 13207–13215.
92 D. Marx, *ChemPhysChem*, 2007, **8**, 209–210.
93 N. Agmon, *Chem. Phys. Lett.*, 1995, **244**, 456–462.
94 M. E. Tuckerman, D. Marx and M. Parrinello, *Nature*, 2002, **417**, 925–929.
95 M. F. Calegari Andrade, H.-Y. Ko, L. Zhang, R. Car and A. Selloni, *Chem. Sci.*, 2020, **11**, 2335–2341.
96 G. Tocci and A. Michaelides, *J. Phys. Chem. Lett.*, 2014, **5**, 474–480.
97 H. Mishra, S. Enami, R. J. Nielsen, M. R. Hoffmann, W. A. Goddard and A. J. Colussi, *Proc. Natl. Acad. Sci. U. S. A.*, 2012, **109**, 10228–10232.
98 S. S. Mirvish, *J. Natl. Cancer Inst.*, 1970, **44**, 633–639.
99 T. Lewis, M. Faubel, B. Winter and J. C. Hemminger, *Angew. Chem., Int. Ed.*, 2011, **50**, 10178–10181.
100 V. Buch, A. Milet, R. Vácha, P. Jungwirth and J. P. Devlin, *Proc. Natl. Acad. Sci. U. S. A.*, 2007, **104**, 7342–7347.
101 S. Enami, M. R. Hoffmann and A. J. Colussi, *J. Phys. Chem. Lett.*, 2010, **1**, 1599–1604.
102 J. Zhong, M. Kumar, J. S. Francisco and X. C. Zeng, *Acc. Chem. Res.*, 2018, **51**, 1229–1237.
103 C. Zhu, M. Kumar, J. Zhong, L. Li, J. S. Francisco and X. C. Zeng, *J. Am. Chem. Soc.*, 2016, **138**, 11164–11169.
104 M. Kumar, H. Li, X. Zhang, X. C. Zeng and J. S. Francisco, *J. Am. Chem. Soc.*, 2018, **140**, 6456–6466.
105 M. T. C. Martins-Costa, J. M. Anglada, J. S. Francisco and M. F. Ruiz-Lopez, *Angew. Chem., Int. Ed.*, 2012, **51**, 5506.
106 N. Myllys, T. Ponkkonen, S. Chee and J. Smith, *Atmosphere*, 2020, **11**, 35.
107 C. Kuang, P. H. McMurry and A. V. McCormick, *Geophys. Res. Lett.*, 2009, **36**, L09822.
108 R. Zhang, A. Khalizov, L. Wang, M. Hu and W. Xu, *Chem. Rev.*, 2012, **112**, 1957–2011.
109 S. Chee, N. Myllys, K. C. Barsanti, B. M. Wong and J. N. Smith, *J. Phys. Chem. A*, 2019, **123**, 5640–5648.